

Geophysical Research Letters®



RESEARCH LETTER

10.1029/2023GL103590

Filtering of Magnetosonic Waves by Mesoscale Plasmaspheric Density Interfaces

Zhiyong Wu^{1,2,3} , Zhenpeng Su^{1,2,3} , Huinan Zheng^{1,2,3} , and Yuming Wang^{1,2,3} 

¹Deep Space Exploration Laboratory, School of Earth and Space Sciences, University of Science and Technology of China, Hefei, China, ²CAS Center for Excellence in Comparative Planetology, CAS Key Laboratory of Geospace Environment, Mengcheng National Geophysical Observatory, University of Science and Technology of China, Hefei, China, ³Collaborative Innovation Center of Astronautical Science and Technology, Hefei, China

Key Points:

- A tens of wavelength wide plasmaspheric density interface separated the magnetosonic waves with differing intensity and frequency coverage
- The local proton Bernstein instabilities are unable to explain the drastic differences between magnetosonic waves in neighboring regions
- The mesoscale plasmaspheric density interfaces can filter the inward penetrating magnetosonic waves in both frequency and incident angle

Supporting Information:

Supporting Information may be found in the online version of this article.

Correspondence to:

Z. Su,
szpe@mail.ustc.edu.cn

Citation:

Wu, Z., Su, Z., Zheng, H., & Wang, Y. (2023). Filtering of magnetosonic waves by mesoscale plasmaspheric density interfaces. *Geophysical Research Letters*, 50, e2023GL103590. <https://doi.org/10.1029/2023GL103590>

Received 7 MAR 2023
Accepted 25 MAY 2023

Abstract Magnetosonic waves inside and outside the plasmasphere differ statistically in occurrence rate, frequency, and intensity. How the density interface separates magnetosonic waves inside and outside the plasmasphere remains not fully understood. Here we report an experimental test made with the Van Allen Probes mission from the plasmaspheric plume through the low-density channel to the plasmaspheric core. Our linear instability analysis and two-dimensional full-wave modeling support that the magnetosonic waves propagate from elsewhere to the channel, undergo reflection and transmission at the flanking plasmaspheric density interfaces and eventually exhibit drastic differences in intensity and frequency coverage between neighboring regions. Such a mesoscale (tens of wavelength wide) interface with a strong refractive index gradient allows the transformation of incident waves to surface waves and consequently filters waves in both frequency and orientation. This unexpected filtering pattern could commonly occur at the plasmaspheric boundary and eventually affect the global distribution of magnetosonic waves.

Plain Language Summary Magnetosonic waves play an important role in the coupling between the ionosphere and magnetosphere and the evolution of the magnetospheric radiation environment. Previous global surveys have shown that magnetosonic waves inside and outside the plasmasphere differ significantly in occurrence rate, frequency, and intensity. In fact, magnetosonic waves are not confined near the source region but are able to propagate over a broad range of radial distances and magnetic local times. An obvious question arises as to how the density interface separates magnetosonic waves inside and outside the plasmasphere. Previous modeling and analysis suggested that the mesoscale (tens of wavelengths) density interface allowed the free penetration of magnetosonic waves from outside to inside the plasmasphere. In contrast, our data and modeling here show that such a mesoscale interface with a strong refractive index gradient allows the transformation of incident waves to surface waves and consequently filters waves in both frequency and incident angle. This unexpected filtering pattern could commonly occur at the plasmaspheric boundary and eventually affect the global distribution of magnetosonic waves.

1. Introduction

In the Earth's inner magnetosphere, magnetosonic waves refer to highly compressional, nearly linearly polarized electromagnetic waves at frequencies from several to hundreds of hertz (Boardsen et al., 2018; Gao et al., 2021; Russell et al., 1970; Santolík et al., 2004; Tsurutani et al., 2014; X. Yu, Yuan, Yao, et al., 2021). Through cyclotron resonance (S. Curtis, 1985; Horne et al., 2000; Ma, Li, Yue, et al., 2019; Sun et al., 2017; Yuan, Yu, et al., 2018), magnetosonic waves can heat thermal ions of ionospheric origin and produce a warm plasma cloak (Asamura et al., 2021; Hill et al., 2020; Olsen, 1981). Through Landau resonance (Fu et al., 2019; Horne et al., 2007; J. Li et al., 2016; L. Y. Li et al., 2017; Xiao et al., 2015), transit-time scattering (Bortnik & Thorne, 2010; Bortnik et al., 2015; J. Li et al., 2014; J. Yu et al., 2019; X. Yu et al., 2020), bounce resonance (Chen et al., 2015; Maldonado & Chen, 2018; Shprits, 2016; Tao & Li, 2016), or even cyclotron resonance (Wu, Su, He, et al., 2022), magnetosonic waves can accelerate or scatter the Van Allen radiation belt electrons.

Magnetosonic waves inside and outside the plasmasphere differ statistically in occurrence rate, frequency, and intensity (Ma, Li, Bortnik, et al., 2019; Ma et al., 2013; Meredith et al., 2008). The Bernstein-mode instabilities of protons (Boardsen et al., 1992; Curtis & Wu, 1979; Gary et al., 2010; K. Liu et al., 2011; Xiao et al., 2013) or other species of ions (Claudepierre et al., 2021; H. Liu et al., 1994; Min et al., 2017) excite magnetosonic waves.

© 2023. The Authors.

This is an open access article under the terms of the [Creative Commons Attribution License](https://creativecommons.org/licenses/by/4.0/), which permits use, distribution and reproduction in any medium, provided the original work is properly cited.

The differences in ion distributions and resonant parameters could lead to the local generation of different magnetosonic waves inside and outside the plasmasphere (Chen et al., 2010; Horne et al., 2000; Kim & Shprits, 2018; Yuan, Ouyang, et al., 2018). However, these waves are not confined near their source regions but are able to propagate over a broad range of radial distances and magnetic local times (Santolík et al., 2016; Santolík, Pickett, Gurnett, Maksimovic, & Cornilleau-Wehrin, 2002; Su et al., 2017; Wu et al., 2021; Xiao et al., 2013). How the density interface separates magnetosonic waves inside and outside the plasmasphere remains not fully understood.

Under the Wentzel-Kramer-Brillouin (WKB) approximation, the plasmopause obstructs the outward spreading of magnetosonic waves within a broad range of azimuthal angles but allows the free inward penetration of magnetosonic waves (Chen & Thorne, 2012; Horne et al., 2000; Kasahara et al., 1994; Santolík et al., 2016; Wu et al., 2021; Xiao et al., 2012). When the plasmopause boundary layer is sufficiently narrow or contains field-aligned density irregularities with a sufficiently small cross-field size, the WKB approximation becomes invalid (X. Liu et al., 2018; X. Yu, Yuan, Ouyang, & Yao, 2021). One-dimensional radial full-wave modeling (X. Liu et al., 2018) suggested that the plasmopause boundary layer had to narrow to the wavelength scale to partially reflect waves, and the embedded subwavelength-scale density irregularities effectively blocked the penetration of waves. In this letter, on the basis of Van Allen Probes observations (Mauk et al., 2013) and two-dimensional full-wave modeling, we show an unexpected filtering effect of the mesoscale (tens of wavelength wide) density interfaces on the magnetosonic waves propagating from outside to inside the plasmasphere. Such a density interface, regardless of whether density irregularities of smaller scales are embedded in, allows the transformation of incident waves to surface waves and then exhibits a transmittance profile dependent on both frequency and orientation.

2. Van Allen Probe Observations

The Van Allen Probes mission contains two identical satellites, RBSP-A and RBSP-B, orbiting the Earth with the perigees ~ 600 km altitude and apogees $\sim 30,000$ km altitude. We use the data from the Electric and Magnetic Field Instrument and Integrated Science suite (EMFISIS; Kletzing et al., 2013), the Electric Field and Waves instrument (EFW; Wygant et al., 2013) and the Energetic particle, Composition and the Thermal plasma suite (ECT; Spence et al., 2013) onboard the mission. Specifically, the ambient magnetic fields are detected by the tri-axial search coil magnetometer (MAG) of EMFISIS; the electromagnetic spectral matrices of waves from 2 Hz to 12 kHz are obtained from the Waveform Receiver (WFR) of EMFISIS; the cold electron density is derived from the upper hybrid frequency (Kurth et al., 2015) measured by the High Frequency Receiver (HFR) of EMFISIS; the satellite electric potential, as a high-resolution proxy of electron density (Wu, Su, Goldstein, et al., 2022; Wygant et al., 2013), is measured by EFW; the energetic proton fluxes of 0.1–700 keV are measured by the Helium Oxygen Proton Electron Mass Spectrometer (HOPE; Funsten et al., 2013) and the Magnetic Electron Ion Spectrometer (MagEIS; Blake et al., 2013) of ECT. Using the previously-proposed techniques (Santolík, Pickett, Gurnett, & Storey, 2002; Santolík et al., 2003, 2010), we calculate the wave normal angles, ellipticities and Poynting fluxes from the provided spectral matrices.

During 15–17 August 2013, the magnetosphere experienced a moderate geomagnetic storm and a series of substorms (Figures 1a and 1b). On 17 August 2013, RBSP-A observed two plasmaspheric plumes in the noon-dusk-midnight sector (Figure 1c). As discussed by Goldstein et al. (2005), the broad plume was likely created by the global convection electric field, while the narrow plume was likely created by the subauroral polarization stream electric field (Foster & Burke, 2002). In the channel between the plasmaspheric core and the narrow plume (Figure 1d), RBSP-A detected magnetosonic waves in the approximately fixed frequency range of 160–330 Hz (Figure 1e). These waves characteristically had normal angles close to 90° and ellipticities close to 0 (Figures 1f and 1g). In contrast, inside the plasmaspheric plume and core, the magnetosonic waves visually narrowed to the frequency range below 260 Hz and their Poynting fluxes decreased by up to several orders of magnitude (Figure 1e). An obvious question arises as to why the magnetosonic waves in such neighboring regions differed so significantly in frequency and power.

One possibility is that magnetosonic waves were locally excited at different frequencies with different powers in different regions. We input the measured proton phase space density (Figure 2a), cold electron density and magnetic field strength to our previously-developed code (N. Liu et al., 2018a, 2018b; Su et al., 2018) and obtain the linear growth rates of magnetosonic waves at a quasi-perpendicular normal angle $\psi = 89.5^\circ$ (Figure 2b). In the plasmaspheric plume, the Alfvén energy E_A was far below the proton ring energy E_R , unfavorable for the effective

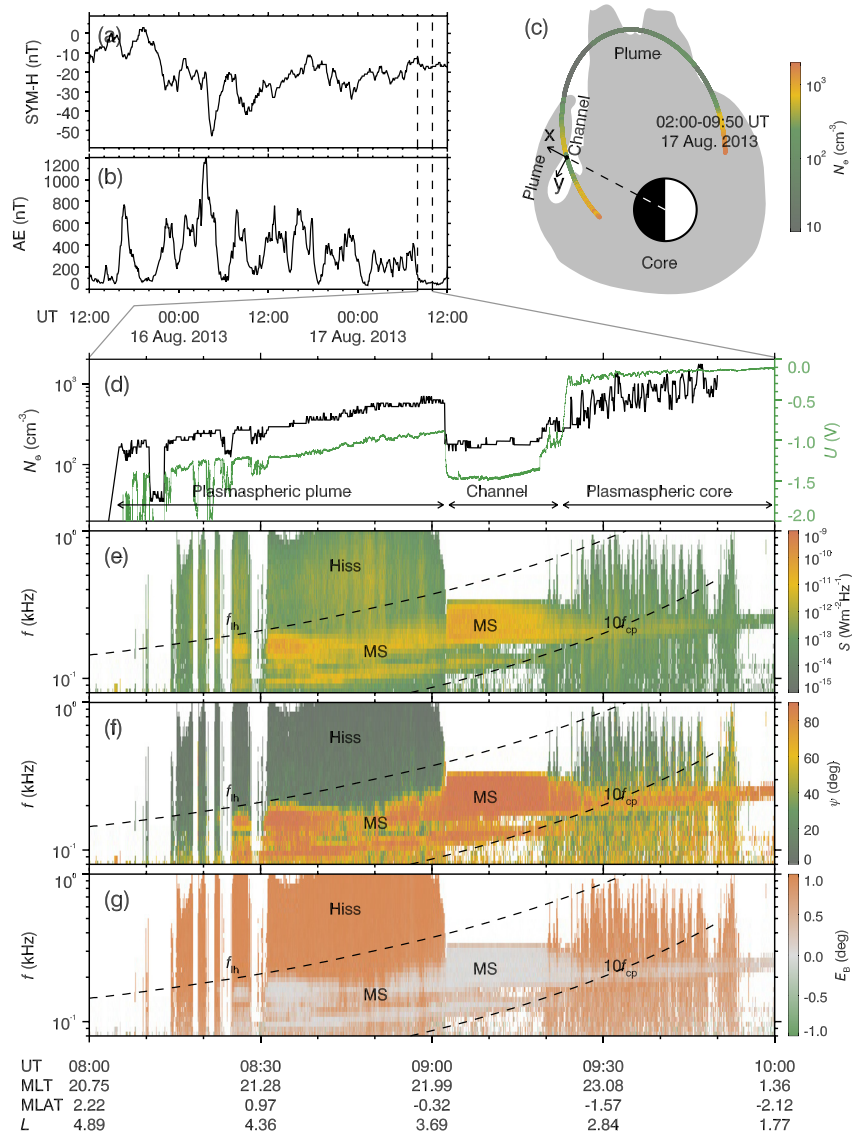


Figure 1. Overview of magnetosonic waves measured by RBSP-A close to the plasmaspheric boundary. Geomagnetic indices (a) SYM-H and (b) AE during 15–17 August 2013. (c) Equatorial plasmaspheric morphology (gray shadow) envisioned from the local density measurements (color-coded) in orbit during 02:00–10:00 UT on 17 August 2013. (d) Cold electron density and satellite potential as well as (e) wave Poynting flux magnitude S , (f) normal angle ψ , and (g) ellipticity E_β during 08:00–10:00 UT on 17 August 2013. In (d–g), the dashed curves represent the lower hybrid frequency f_{lh} and 10th harmonic of the proton cyclotron frequency f_{cp} .

growth of magnetosonic waves. The modeled convective growth of waves is allowed with a quite low rate of $\sim 10^{-8} \text{ m}^{-1}$ in the frequency range roughly below 200 Hz. In the channel with density depletion, although the Alfvén energy has increased, the growth rates of magnetosonic waves from the weak proton rings remain insufficiently high. Moreover, the wave growth rates peak at lower frequencies than the observed magnetosonic waves (Figure 2c). In the plasmaspheric core without observable proton rings, no magnetosonic waves are allowed to grow effectively. These results do not support the local generation of magnetosonic waves in the spatial regions of interest.

Another possibility is that the spatial dependence of magnetosonic waves was a consequence of their reflection and transmission at the density interfaces. We speculate that the magnetosonic waves originated from the plasmatrough that was connected to the channel. Compared to the channel, the plasmatrough could have stronger proton rings, Alfvén energies closer to the ring energies, and higher growth rates of magnetosonic waves. The repeated reflections and transmissions at the channel boundaries on both sides eventually disordered the azimuthal angles

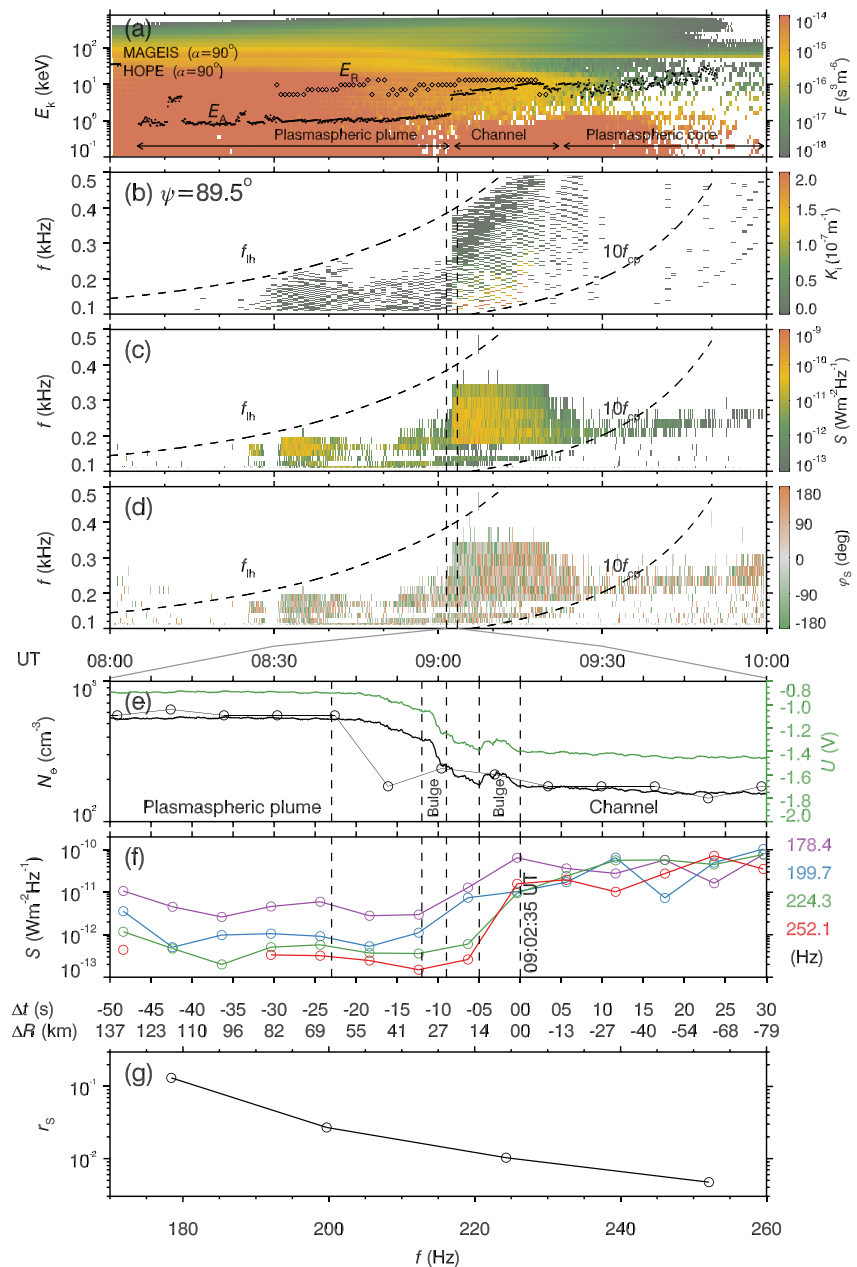


Figure 2. Instability and propagation of magnetosonic waves. (a) Proton phase space density F at 90° pitch-angle, overlain by the Alfvén energy E_A (dots) and ring energy E_R (rhombus). (b) Convective growth rate K_i at the normal angle $\psi = 89.5^\circ$. (c) Magnitude S and (d) azimuthal angle φ_s of Poynting flux. Only the waves with magnetic power spectral densities $P_B > 10^{-8} \text{ nT}^2 \text{ Hz}^{-1}$, normal angles $\psi > 75^\circ$, ellipticities $|E_B| < 0.5$ are shown. $\varphi_s = 0^\circ$ and $\varphi_s = 90^\circ$ correspond to the anti-earthward and eastward propagation of waves. Magnified view of the (e) cold electron density N_e and (f) wave Poynting fluxes at different frequencies (indicated). The cold electron density derived from the upper hybrid frequency (black circles connected by a thin line) has a much lower temporal resolution than that derived from the satellite potential (black thick line). The time difference Δt relative to 09:02:35 UT and radial distance away from the plume boundary ΔR are labeled below. (g) Frequency-dependent ratio r_s between wave Poynting fluxes inside and outside the plasmaspheric plume.

of wave Poynting fluxes (Figure 2d). As shown by the low-resolution density profile of HFR (Figure 2e), the plume boundary layer (09:02:12–09:02:32 UT) had a width of $\sim 50 \text{ km}$ (~ 10 – 30 times the nearby magnetosonic wave wavelength in the channel). By fitting the density data of HFR, we obtain the high-resolution density profile from the satellite potential of EFW

$$N_e = C_1 e^{C_3 U} + C_2 e^{C_4 U} \quad (1)$$

with $C_1 = 1951.1 \text{ cm}^{-3}$, $C_2 = 1939.5 \text{ cm}^{-3}$, $C_3 = 2.25 \text{ V}^{-1}$, and $C_4 = 2.16 \text{ V}^{-1}$. We find two density bulges with radial widths of $\sim 14 \text{ km}$ ($\sim 2\text{--}9$ times the nearby magnetosonic wave wavelength in the channel) embedded in the plume boundary layer. Near the foot of the plume boundary layer, the wave Poynting fluxes decreased sharply and dispersively (Figure 2f). To characterize magnetosonic wave weakening, we introduce an energy ratio parameter

$$r_s = \frac{\overline{S_{\text{pl}}}}{\overline{S_{\text{ch}}}}, \quad (2)$$

where $\overline{S_{\text{pl}}}$ and $\overline{S_{\text{ch}}}$ are 30 s-averaged Poynting flux magnitudes in the plume (09:01:40–09:02:10 UT) and channel (09:02:40–09:03:10 UT). r_s monotonically decreased from 0.132 at 178.4 Hz to 0.005 at 252.1 Hz (Figure 2g). Above 252.1 Hz, r_s is unavailable because the corresponding wave Poynting fluxes had fallen to the noise level in the plume. Such a frequency-dependent weakening of magnetosonic wave power also occurred in the plasmaspheric core (Figure 2c). Compared to the plume boundary layer, the core boundary layer (09:20–09:50 UT) was wider and contained more prominent density irregularities (Figure 1d). These observations imply that higher-frequency (shorter-wavelength) magnetosonic waves had smaller transmission rates. This frequency dependency does not seem to be in line with the intuition that the propagation of lower-frequency (longer-wavelength) waves is more likely to be obstructed by density structures.

3. Two-Dimensional Full-Wave Modeling

We next investigate the behavior of magnetosonic waves near these density interfaces on the basis of full-wave modeling. The wave electromagnetic fields \mathbf{E} and \mathbf{B} are determined by Maxwell's equations.

$$\nabla \times \mathbf{E} = -\frac{\partial \mathbf{B}}{\partial t}, \quad (3)$$

$$\nabla \times \mathbf{B} = \epsilon_0 \mu_0 \frac{\partial \mathbf{E}}{\partial t} + \mu_0 \sum_{\alpha} \mathbf{J}_{\alpha} \quad (4)$$

with the vacuum permeability μ_0 and permittivity ϵ_0 . The electric current densities \mathbf{J}_{α} carried by electrons ($\alpha = e$) and protons ($\alpha = p$) are determined by the linearized momentum equations

$$\frac{\partial \mathbf{J}_{\alpha}}{\partial t} + \nu_{\alpha} \mathbf{J}_{\alpha} = \epsilon_0 \omega_{p\alpha}^2 \mathbf{E} - \mathbf{\Omega}_{c\alpha} \times \mathbf{J}_{\alpha} \quad (5)$$

with the collision frequency ν_{α} , plasma frequency $\omega_{p\alpha}$, and cyclotron frequency vector $\mathbf{\Omega}_{c\alpha}$ for α species. We solve the equations above with a modified finite-difference-time-domain method (e.g., X. Liu et al., 2018; Streltsov et al., 2006; Williams, 2014; Xu et al., 2020; Yang et al., 2011).

Compared with the plasmaspheric core boundary layer with multiscale nested density irregularities, the plasmaspheric plume boundary layer had a more structured and composable density profile. Without loss of generality, we perform specific modeling under the spatial context of the plume boundary layer. To reduce the computational cost, we assume that magnetosonic waves are propagating with a fixed normal angle $\psi = 90^\circ$ in the equatorial plane. We define a local Cartesian coordinate system (Figure 1b) with the origin at the site of RBSP-A at 09:02:35 UT, the x -axis along the radial direction, the z -axis parallel to the magnetic field, and the y -axis completing the right-hand rule. For magnetosonic waves of 100–330 Hz, the magnetosonic wavelengths λ_{ch} in the channel range from 2 to 10 km. For a specific wave, the computational domain is located in a square with $\Delta x = \Delta y = 100\lambda_{\text{ch}}$. Within such a limited spatial region, we assume a constant background magnetic field \mathbf{B}_0 of 600 nT in the z direction (corresponding to the RBSP-A observation at 09:02:30 UT in Figure 2). Considering that the wave power was observed to change significantly near the channel boundary, we have ignored the density bulge embedded in the middle of the boundary layer. Neglecting the density variation tangential to the plume, we assume an x -dependent electron density profile N_e by fitting to EFW data (Figures 3a and 3b).

$$N_e = N_0 + N_{\text{bg}}, \quad (6)$$

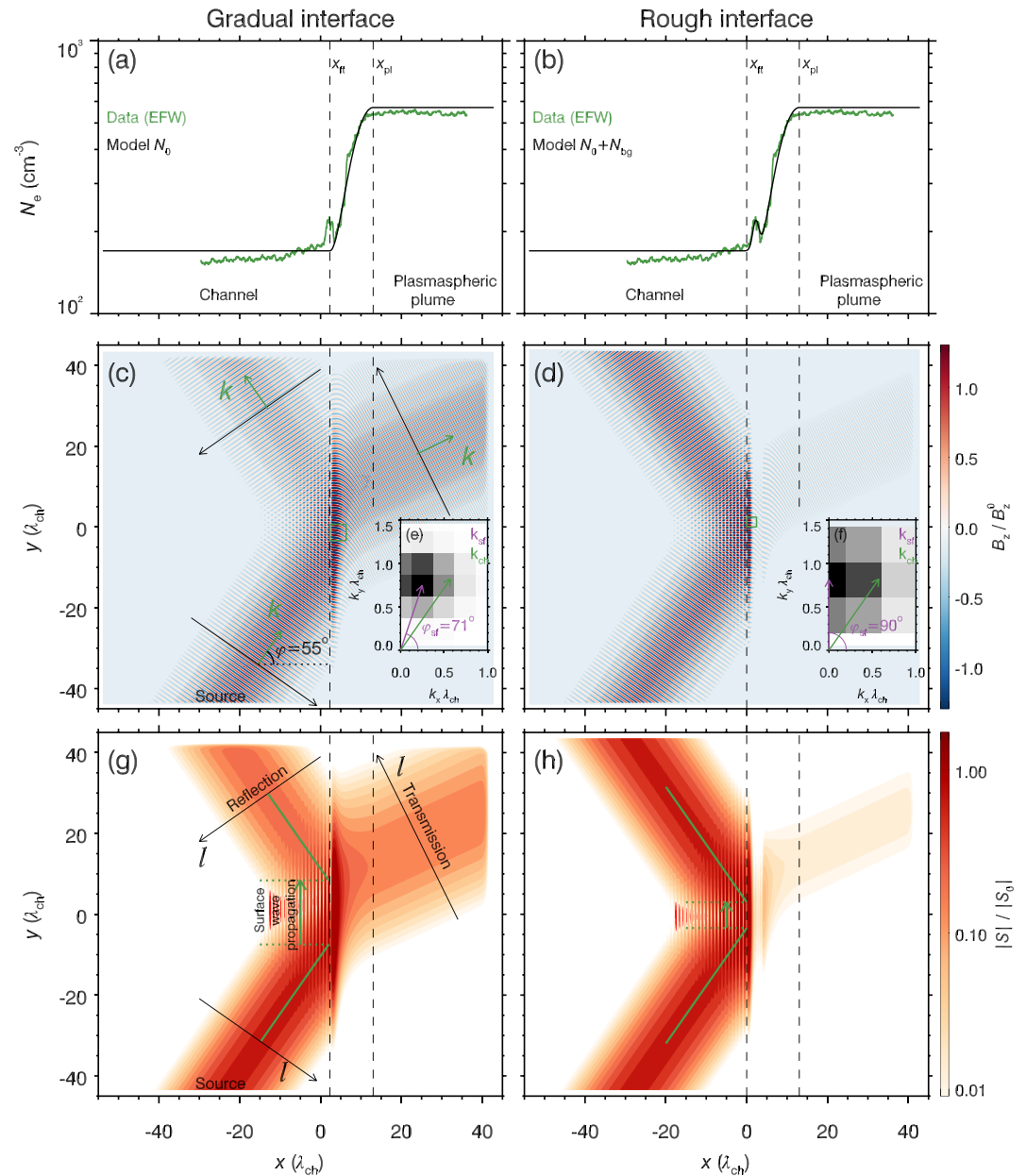


Figure 3. Two-dimensional full-wave modeling of the propagation of magnetosonic waves with the frequency $f = 178.4$ Hz and incident angle $\varphi = 55^\circ$ at the gradual (left) and rough (right) density interfaces. (a and b) Modeled (black) and observed (green) electron density. (c and d) Normalized magnetic waveform B_z/B_0^0 , with the green arrows indicating the wavevector directions and the black arrows indicating the wavefront. The waveform data in green rectangles are used for the spatial fast Fourier transform. (e and f) Spatial fast Fourier transform spectra scaled by the magnitude of black saturation. The spectral peak locations indicate the wavevectors \mathbf{k}_{sf} inside the interface (purple arrows), in comparison to the wavevectors \mathbf{k}_{ch} in the channel (green arrows). The spectral grid size represents the error range of the calculated \mathbf{k}_{sf} . (g and h) Normalized Poynting flux magnitude $|S|/|S_0|$, with the green lines indicating the beam centers of incident and reflected waves.

$$N_0 = \begin{cases} 170 & x \leq x_{bg}, \\ 205 \cos\left(\frac{x - x_{pl}}{x_{pl} - x_{bg}} \pi\right) + 375 & x_{bg} < x \leq x_{pl}, \\ 580 & x > x_{pl}, \end{cases} \quad (7)$$

$$N_{\text{bg}} = 50 \exp \left[-100 \left(\frac{x - x_{\text{bg}}}{x_{\text{pl}} - x_{\text{bg}}} \right)^2 \right], \quad (8)$$

where N_0 and N_{bg} (in unit of cm^{-3}) represent the components for the background gradual interface and small-scale density bulge, x_{bg} is the bulge center, and x_{pl} is the inner edge of the boundary layer. All these density parameters are independent of wavelength and incident angle and fixed in the following simulations. For the gradual interface without the density bulge, its foot is $x_{\text{ft}} = x_{\text{bg}}$; for the rough interface with the density bulge, its foot x_{ft} steps back ~ 10 km from x_{bg} .

In the coordinate system defined above, magnetosonic waves have three electromagnetic components B_z , E_x , and E_y . At a horizontal line $y = y_s$, we launch magnetosonic waves by specifying

$$B_z(x, y_s) = B_z^0 \exp \left[- \left(\frac{x - x_s}{w_s} \right)^2 \right] \sin \left(\int k_x dx - \omega t \right), \quad (9)$$

where B_z^0 is the peak amplitude in the channel, x_s and w_s are the center and width of the Gaussian wave source, $k_x = k \cos \varphi$ is the parallel wavenumber from the cold plasma wave theory, and φ is the incident angle. With $w_s = 15\lambda_{\text{ch}}$, the wave amplitude varies quite slowly along the wavefront. The freshly launched waves could be approximated as plane waves. Near the boundary of the modeling domain, the collision frequency ν_α gradually increases from 0 to a sufficiently large value to absorb the waves (X. Liu et al., 2018; Xu et al., 2020). The wave Poynting flux is defined as

$$\mathbf{S}(x, y, t) = \frac{1}{\mu_0 T} \int_{t-T}^t \mathbf{E}(x, y, \tau) \times \mathbf{B}(x, y, \tau) d\tau \quad (10)$$

with the wave period T . When the modeling system reaches the steady state, \mathbf{S} is nearly independent of t . The launched, reflected and transmitted wave power are defined as integrals of the Poynting flux along the wavefront

$$\langle S \rangle = \int |\mathbf{S}| dl \quad (11)$$

with the integral path \mathbf{l} perpendicular to the wavevector \mathbf{k} that is oriented along the major axis of the electric field polarization ellipsoid (Laakso et al., 1990). The reflection (transmission) coefficient C_R (C_T) are determined as the ratio between reflected (transmitted) and launched wave power.

In Figure 3, we present a comparison of the waveform and Poynting flux of the magnetosonic waves at the gradual and rough interfaces. These magnetosonic waves are launched with frequency $f = 178.4$ Hz and incident angle $\varphi = 55^\circ$. It can be found that, once the incident plane wave penetrates the interface foot, its wavefront is abruptly bent toward the y -direction (Figures 3c and 3d). This deformed wave just inside the interface may be interpreted as a type of surface wave. Electromagnetic waves have long been known to propagate as surface waves if they can be “guided” by a grad-refractive-index medium or by an interface between two different media (Polo et al., 2013). We identify the position $[x_p, y_p]$ with the peak Poynting flux (Figures 3g and 3h) inside the interface and define the skin depth D_{sf} of the surface wave as the distance between the interface foot (x_{ft}, y_p) and the position ($x > x_p, y_p$) with the Poynting flux dropping to $|\mathbf{S}(x_p, y_p)|/e$. The identified skin depths of surface waves are 10 and 5 km at the gradual and rough interfaces, comparable to the wavelength of 5 km in the channel. In Figures 3e and 3f, we calculate the surface wavevector \mathbf{k}_{sf} by the spatial fast Fourier transform of B_z in the spatial domain $\{x \in [x_{\text{ft}}, x_{\text{ft}} + 2D_{\text{sf}}], y \in [y_p - D_{\text{sf}}, y_p + D_{\text{sf}}]\}$. Clearly, for both types of interfaces, the obtained parallel wavenumbers k_x of the surface waves are much smaller than the incident ones. In contrast, the corresponding two perpendicular wavenumbers k_y are consistent within the error range, which can be confirmed visually from the waveforms (Figures 3c and 3d). Because the waves just inside and outside the interface are in the same perpendicular phase, the incident wave continuously supplies energy to the propagating surface wave. Meanwhile, the surface wave create an alternating current system with the same frequency (Figure S1 in Supporting Information S1), which further emits waves toward both sides. Toward the outside, the emitted wave with the fixed f and k_y is essentially the reflected magnetosonic wave. Inside the interface, the density gradient corresponds to a gradient in the wave phase velocity. Along with the propagation of surface wave, its wavefront tilts and k_x increases. When k_x becomes sufficiently large, the emitted wave can travel through the subsequent

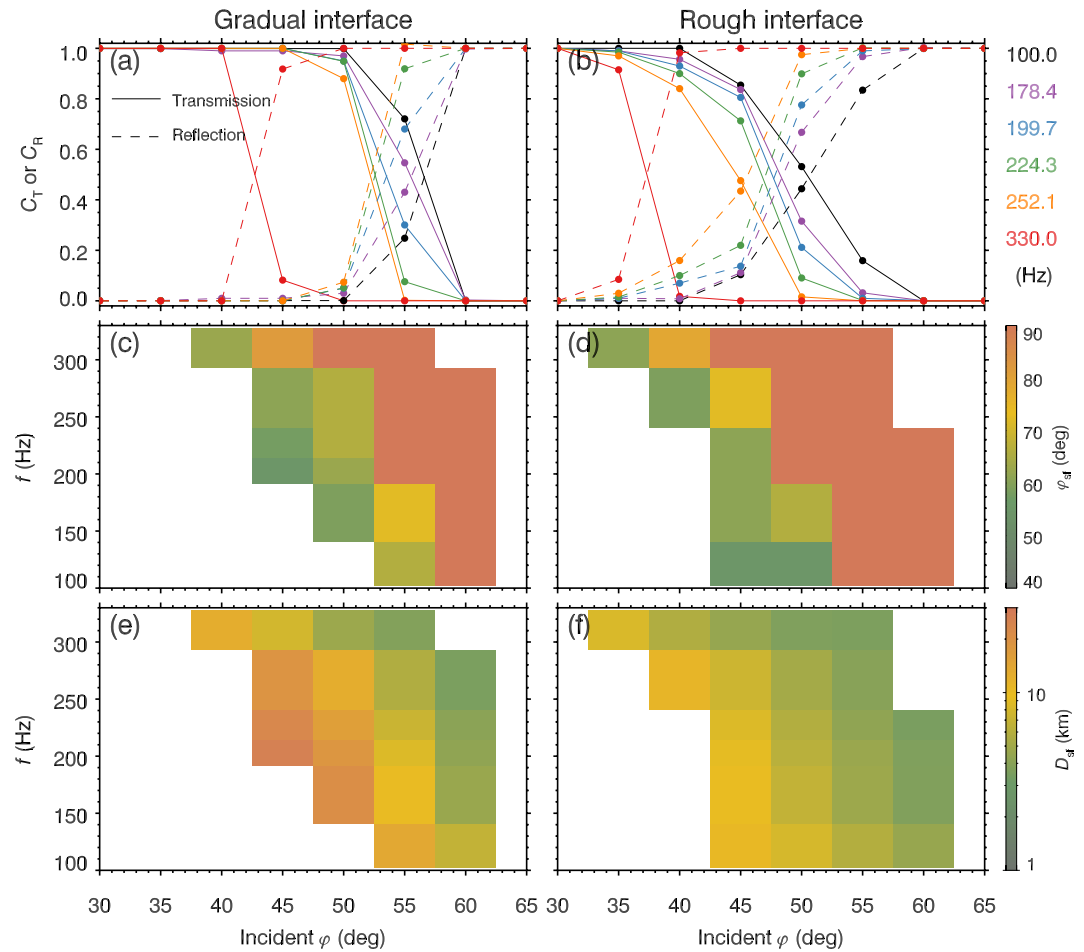


Figure 4. Dependence of magnetosonic wave propagation characteristics on frequency and incident angle at the gradual (left) and rough (right) density interfaces. (a and b) Transmission (solid lines) and reflection (dashed lines) coefficients C_T and C_R . (c and d) Surface wave azimuthal angle φ_{sf} and (e and f) skin depth D_{sf} , with the blank regions denoting D_{sf} larger than half of the interface layer width or lower than one wavelength. An overlage D_{sf} indicates that the surface wave does not form; a too-small D_{sf} is not conducive to the wavevector calculation.

density gradient and becomes the transmitted magnetosonic wave. The simultaneous propagation and leakage of the surface wave and its external driving by the incident wave collectively lead to the spatial broadening of the reflected and transmitted beams and the shift of their centers along the y -direction at the interface (Figures 3c and 3d). Regardless of whether the density bulge is included, the partial reflection and transmission of magnetosonic waves mainly occur at the foot of the interface, consistent with observations (Figures 2e and 2f). The inclusion of a density bulge reduces the surface wave depth and causes the reflection coefficient to increase from 45% to 96%. Because the surface waves are actually confined near the interface foot, the density gradient at the interface foot is a critical parameter to control the reflection and transmission coefficients (see the additional tests in Figure S2 in Supporting Information S1).

In Figure 4, we investigate the dependence of wave propagation characteristics on frequency f and incident angle φ . For the magnetosonic waves of interest, the transmission (reflection) coefficients are negatively (positively) related to the frequency and incident angle at both the gradual and rough interfaces (Figures 4a and 4b). At a fixed frequency, k_y increases with the incident angle. Because the surface wave has to propagate along the y -direction, the increase of k_y promotes the surface wave development, which is manifest in the dependence of both wavevector direction (Figures 4c and 4d) and skin depth (Figures 4e and 4f) on the incident angle. A more significant surface wave corresponds to a stronger reflection. At the sufficiently small incident angles, the surface waves are ignorable and the interfaces are nearly transparent; in contrast, when the surface waves develop substantially at the intermediate and large incident angles, the interfaces become translucent or opaque.

In view of the observed energy ratio of 0.1 or less between waves in the plume and channel (Figure 2g), we speculate that the magnetosonic waves on average had incident angles of 40° – 60° . Similarly, at a fixed incident angle, k_y increases with the wave frequency and higher-frequency waves have larger reflection coefficients, which is responsible for the frequency dependence of the observed plume-to-channel energy ratio of magnetosonic waves (Figures 2f and 2g). Compared to the gradual interface, the rough interface has a larger density gradient near the foot and reflects the magnetosonic waves more strongly over a broader range of frequencies and incident angles.

4. Conclusion and Discussion

On the basis of data and modeling, we find an unexpected filtering effect of the mesoscale density interfaces on the magnetosonic waves propagating from outside to inside the plasmasphere. Within 1 hr, Van Allen Probe A crossed the plasmaspheric plume and core separated by a low-density channel in the pre-midnight sector. Compared to the channel, the plasmaspheric plume and core had magnetosonic waves with weaker Poynting fluxes and in a narrower frequency range. Our linear instability analysis indicates that, in the sampling regions, the local growth rates of magnetosonic waves are at an extremely low level and exhibit different frequency-dependence characteristics from their Poynting fluxes. We speculate that these waves propagated from the plasmatrough into the channel and experienced reflections and transmissions at the density interfaces. Our two-dimensional full-wave modeling demonstrates that, contrary to the prediction of previous modeling and analysis, such a density interface with a width of tens of wavelengths is translucent or opaque for magnetosonic waves with sufficiently large incident angles. Somewhat counterintuitively, the reflection is more significant for waves with smaller wavelengths in the frequency range of interest. Our modeled filtering for the magnetosonic waves with incident angles of 40° – 60° can reasonably explain the observed frequency-dependent variations of wave Poynting fluxes across the density interface.

The filtering pattern described above is caused by the transformation of incident waves into surface waves near the interface foot. The corresponding density gradient is a critical parameter controlling the reflection and transmission coefficients. The incident waves with larger wavenumbers along the interface are more prone to transformation into surface waves. The incident wavenumber is positively related to the frequency and incident angle. As a result, the density interface filters the magnetosonic waves in both frequency and orientation. This filtering pattern does not necessarily require the embedment of density irregularities in the density interface. Compared to the gradual interface, the rough interface with a density bulge has a larger density gradient at the foot and reflects the magnetosonic waves more significantly over a broader range of frequencies and incident angles.

Because of the rotation, erosion, and filling processes, the plasmasphere exhibits diverse structures and boundaries over a broad range of radial distances and magnetic local times (Borovsky & Denton, 2008; Darrouzet et al., 2009; Goldstein et al., 2004). Meanwhile, these boundaries are rich in density irregularities of smaller scales (Carpenter & Lemaire, 1997; Carpenter et al., 2002; Gu et al., 2022; Thomas et al., 2021; Wu, Su, Goldstein, et al., 2022). The incidence of magnetosonic waves toward density interfaces should frequently occur and the associated transmission and reflection processes would eventually affect the global distribution of magnetosonic waves. According to the event-specific observations, our present modeling concentrates on the tens of wavelength wide density interfaces and the several wavelength wide density irregularities. The variation in the spatial scale of density interfaces and irregularities could significantly change the transmission and reflection coefficients of magnetosonic waves. Our present modeling has simplified the density irregularity as a one-dimensional radial density oscillation. In fact, it may be more appropriate to interpret the density irregularity as a field-aligned density tube (Carpenter et al., 2002; Loi et al., 2015; Sonwalkar, 2006). At the plasmaspheric boundary, a group of density irregularities could form a grating-like system, potentially allowing diffraction and interference of waves (Woodroffe & Streltsov, 2014). More parametric studies on the propagation of magnetosonic waves near structured density interfaces are left for future work.

Data Availability Statement

Van Allen Probes data are available at <https://spdf.gsfc.nasa.gov/pub/data/rbsp/>; SYM-H and AE data are available at <http://wdc.kugi.kyoto-u.ac.jp/wdc/Sec3.html>.

Acknowledgments

We acknowledge EMFISIS, EFW, and ECT teams for the use of Van Allen Probes data and WDC for Geomagnetism (Kyoto) for the use of the SYM-H and AE indices. This work was supported by the Strategic Priority Research Program of Chinese Academy of Sciences Grant XDB 41000000, the National Natural Science Foundation of China Grants 42130204, 42188101, and 42274198, and the Key Research Program of the Chinese Academy of Sciences Grant ZDRE-KT-2021-3.

References

- Asamura, K., Shoji, M., Miyoshi, Y., Kasahara, Y., Kasaba, Y., Kumamoto, A., et al. (2021). Cross-energy couplings from magnetosonic waves to electromagnetic ion cyclotron waves through cold ion heating inside the plasmasphere. *Physical Review Letters*, *127*(24), 245101. <https://doi.org/10.1103/PhysRevLett.127.245101>
- Blake, J. B., Carranza, P. A., Claudepierre, S. G., Clemmons, J. H., Crain, W. R., Dotan, Y., et al. (2013). The magnetic electron ion spectrometer (MagEIS) instruments aboard the radiation belt storm probes (RBSP) spacecraft. *Space Science Reviews*, *179*(1–4), 383–421. <https://doi.org/10.1007/s11214-013-9991-8>
- Boardsen, S. A., Gallagher, D. L., Gurnett, D. A., Peterson, W. K., & Green, J. L. (1992). Funnel-shaped, low-frequency equatorial waves. *Journal of Geophysical Research*, *97*(A10), 14. <https://doi.org/10.1029/92JA00827>
- Boardsen, S. A., Hospodarsky, G. B., Min, K., Averkamp, T. F., Bounds, S. R., Kletzing, C. A., & Pfaff, R. F. (2018). Determining the wave vector direction of equatorial fast magnetosonic waves. *Geophysical Research Letters*, *45*(16), 7951–7959. <https://doi.org/10.1029/2018GL078695>
- Borovsky, J. E., & Denton, M. H. (2008). A statistical look at plasmaspheric drainage plumes. *Journal of Geophysical Research*, *113*(A9), A09221. <https://doi.org/10.1029/2007JA012994>
- Bortnik, J., & Thorne, R. M. (2010). Transit time scattering of energetic electrons due to equatorially confined magnetosonic waves. *Journal of Geophysical Research*, *115*(A7), A07213. <https://doi.org/10.1029/2010JA015283>
- Bortnik, J., Thorne, R. M., Ni, B., & Li, J. (2015). Analytical approximation of transit time scattering due to magnetosonic waves. *Geophysical Research Letters*, *42*(5), 1318–1325. <https://doi.org/10.1002/2014GL026710>
- Carpenter, D. L., & Lemaire, J. (1997). Erosion and recovery of the plasmasphere in the plasmopause region. *Space Science Reviews*, *80*(1/2), 153–179. <https://doi.org/10.1023/A:1004981919827>
- Carpenter, D. L., Spasojević, M. A., Bell, T. F., Inan, U. S., Reinisch, B. W., Galkin, I. A., & Boardsen, S. A. (2002). Small-scale field-aligned plasmaspheric density structures inferred from the Radio Plasma Imager on IMAGE. *Journal of Geophysical Research*, *107*(A9), 1258. <https://doi.org/10.1029/2001JA009199>
- Chen, L., Maldonado, A., Bortnik, J., Thorne, R. M., Li, J., Dai, L., & Zhan, X. (2015). Nonlinear bounce resonances between magnetosonic waves and equatorially mirroring electrons. *Journal of Geophysical Research*, *120*(8), 6514–6527. <https://doi.org/10.1002/2015JA021174>
- Chen, L., & Thorne, R. M. (2012). Perpendicular propagation of magnetosonic waves. *Geophysical Research Letters*, *39*(14), L14102. <https://doi.org/10.1029/2012GL052485>
- Chen, L., Thorne, R. M., Jordanova, V. K., & Horne, R. B. (2010). Global simulation of magnetosonic wave instability in the storm time magnetosphere. *Journal of Geophysical Research*, *115*(A11), A11222. <https://doi.org/10.1029/2010JA015707>
- Claudepierre, S. G., Liu, X., Chen, L., & Takahashi, K. (2021). Observational evidence of the excitation of magnetosonic waves by an He++ ion ring distribution. *Journal of Geophysical Research: Space Physics*, *126*(8), e29532. <https://doi.org/10.1029/2021JA029532>
- Curtis, S. (1985). Equatorial trapped plasmasphere ion distributions and transverse stochastic acceleration. *Journal of Geophysical Research*, *90*(A2), 1765–1770. <https://doi.org/10.1029/ja090a02p01765>
- Curtis, S. A., & Wu, C. S. (1979). Gyroharmonic emissions induced by energetic ions in the equatorial plasmasphere. *Journal of Geophysical Research*, *84*(A6), 2597–2607. <https://doi.org/10.1029/JA084iA06p02597>
- Darrrouzet, F., Gallagher, D. L., André, N., Carpenter, D. L., Dandouras, I., Décréau, P. M. E., et al. (2009). Plasmaspheric density structures and dynamics: Properties observed by the CLUSTER and IMAGE missions. *Space Science Reviews*, *145*(1–2), 55–106. <https://doi.org/10.1007/s11214-008-9438-9>
- Foster, J. C., & Burke, W. J. (2002). SAPS: A new categorization for sub-auroral electric fields. *EOS Transactions*, *83*(36), 393. <https://doi.org/10.1029/2002EO000289>
- Fu, S., Ni, B., Zhou, R., Cao, X., & Gu, X. (2019). Combined Scattering of radiation belt electrons caused by Landau and bounce resonant interactions with magnetosonic waves. *Geophysical Research Letters*, *46*(17–18), 10313–10321. <https://doi.org/10.1029/2019GL084438>
- Funsten, H. O., Skoug, R. M., Guthrie, A. A., MacDonald, E. A., Baldonado, J. R., Harper, R. W., et al. (2013). Helium, oxygen, proton, and electron (HOPE) mass spectrometer for the radiation belt storm probes mission. *Space Science Reviews*, *179*(1–4), 423–484. <https://doi.org/10.1007/s11214-013-9968-7>
- Gao, Z., Liu, S., Xiao, F., Zhou, Q., He, Q., Li, T., et al. (2021). Observation and fully thermal simulation of quasi-electrostatic magnetosonic waves. *Geophysical Research Letters*, *48*(24), e95757. <https://doi.org/10.1029/2021GL095757>
- Gary, S. P., Liu, K., Winske, D., & Denton, R. E. (2010). Ion Bernstein instability in the terrestrial magnetosphere: Linear dispersion theory. *Journal of Geophysical Research*, *115*(A12), A12209. <https://doi.org/10.1029/2010JA015965>
- Goldstein, J., Burch, J. L., & Sandel, B. R. (2005). Magnetospheric model of subauroral polarization stream. *Journal of Geophysical Research*, *110*(A9), A09222. <https://doi.org/10.1029/2005JA011135>
- Goldstein, J., Sandel, B. R., Thomsen, M. F., Spasojević, M., & Reiff, P. H. (2004). Simultaneous remote sensing and in situ observations of plasmaspheric drainage plumes. *Journal of Geophysical Research*, *109*, 3202. <https://doi.org/10.1029/2003JA010281>
- Gu, W., Liu, X., Xia, Z., & Chen, L. (2022). Statistical study on small-scale ($\leq 1,000$ km) density irregularities in the inner magnetosphere. *Journal of Geophysical Research: Space Physics*, *127*(7), e30574. <https://doi.org/10.1029/2022JA030574>
- Hill, S., Buzulukova, N., Boardsen, S., & Fok, M. C. (2020). Local heating of oxygen ions in the presence of magnetosonic waves: Possible source for the warm plasma cloak? *Journal of Geophysical Research: Space Physics*, *125*(8), e27210. <https://doi.org/10.1029/2019JA027210>
- Horne, R. B., Thorne, R. M., Glauert, S. A., Meredith, N. P., Pokhotelov, D., & Santolík, O. (2007). Electron acceleration in the Van Allen radiation belts by fast magnetosonic waves. *Geophysical Research Letters*, *34*(17), L17107. <https://doi.org/10.1029/2007GL030267>
- Horne, R. B., Wheeler, G. V., & Alleyne, H. S. C. K. (2000). Proton and electron heating by radially propagating fast magnetosonic waves. *Journal of Geophysical Research*, *105*(A12), 27597–27610. <https://doi.org/10.1029/2000JA000018>
- Kasahara, Y., Kenmochi, H., & Kimura, I. (1994). Propagation characteristics of the ELF emissions observed by the satellite Akebono in the magnetic equatorial region. *Radio Science*, *29*(4), 751–767. <https://doi.org/10.1029/94RS00445>
- Kim, K.-C., & Shprits, Y. (2018). Survey of the favorable conditions for magnetosonic wave excitation. *Journal of Geophysical Research: Space Physics*, *123*(1), 400–413. <https://doi.org/10.1002/2017JA024865>
- Kletzing, C. A., Kurth, W. S., Acuna, M., MacDowall, R. J., Torbert, R. B., Averkamp, T., et al. (2013). The electric and magnetic field instrument suite and integrated science (EMFISIS) on RBSP. *Space Science Reviews*, *179*(1–4), 127–181. <https://doi.org/10.1007/s11214-013-9993-6>
- Kurth, W. S., De Pascuale, S., Faden, J. B., Kletzing, C. A., Hospodarsky, G. B., Thaller, S., & Wygant, J. R. (2015). Electron densities inferred from plasma wave spectra obtained by the Waves instrument on Van Allen Probes. *Journal of Geophysical Research: Space Physics*, *120*(2), 904–914. <https://doi.org/10.1002/2014JA020857>
- Laakso, H., Junginger, H., Schmidt, R., Roux, A., & de Villedary, C. (1990). Magnetosonic waves above $f_c(H^+)$ at geostationary orbit - GEOS 2 results. *Journal of Geophysical Research*, *95*(A7), 10609–10621. <https://doi.org/10.1029/JA095iA07p10609>

- Li, J., Ni, B., Ma, Q., Xie, L., Pu, Z., Fu, S., et al. (2016). Formation of energetic electron butterfly distributions by magnetosonic waves via Landau resonance. *Geophysical Research Letters*, *43*(7), 3009–3016. <https://doi.org/10.1002/2016GL067853>
- Li, J., Ni, B., Xie, L., Pu, Z., Bortnik, J., Thorne, R. M., et al. (2014). Interactions between magnetosonic waves and radiation belt electrons: Comparisons of quasi-linear calculations with test particle simulations. *Geophysical Research Letters*, *41*(14), 4828–4834. <https://doi.org/10.1002/2014GL060461>
- Li, L. Y., Yu, J., Cao, J. B., Yang, J. Y., Li, X., Baker, D. N., et al. (2017). Roles of whistler mode waves and magnetosonic waves in changing the outer radiation belt and the slot region. *Journal of Geophysical Research: Space Physics*, *122*(5), 5431–5448. <https://doi.org/10.1002/2016JA023634>
- Liu, H., Kokubun, S., & Hayashi, K. (1994). Equatorial electromagnetic emission with discrete spectra near harmonics of oxygen gyrofrequency during magnetic storm. *Geophysical Research Letters*, *21*(3), 225–228. <https://doi.org/10.1029/93GL02836>
- Liu, K., Gary, S. P., & Winske, D. (2011). Excitation of magnetosonic waves in the terrestrial magnetosphere: Particle-in-cell simulations. *Journal of Geophysical Research*, *116*(A7), A07212. <https://doi.org/10.1029/2010JA016372>
- Liu, N., Su, Z., Zheng, H., Wang, Y., & Wang, S. (2018a). Magnetosonic harmonic falling and rising frequency emissions potentially generated by nonlinear wave-wave interactions in the Van Allen radiation belts. *Geophysical Research Letters*, *45*(16), 7985–7995. <https://doi.org/10.1029/2018GL079232>
- Liu, N., Su, Z., Zheng, H., Wang, Y., & Wang, S. (2018b). Prompt disappearance and emergence of radiation belt magnetosonic waves induced by solar wind dynamic pressure variations. *Geophysical Research Letters*, *45*(2), 585–594. <https://doi.org/10.1002/2017GL076382>
- Liu, X., Chen, L., Yang, L., Xia, Z., & Malaspina, D. M. (2018). One-dimensional full wave simulation of equatorial magnetosonic wave propagation in an inhomogeneous magnetosphere. *Journal of Geophysical Research: Space Physics*, *123*(1), 587–599. <https://doi.org/10.1002/2017JA024336>
- Loi, S. T., Murphy, T., Cairns, I. H., Menk, F. W., Waters, C. L., Erickson, P. J., et al. (2015). Real-time imaging of density ducts between the plasmasphere and ionosphere. *Geophysical Research Letters*, *42*(10), 3707–3714. <https://doi.org/10.1002/2015GL063699>
- Ma, Q., Li, W., Bortnik, J., Kletzing, C. A., Kurth, W. S., Hospodarsky, G. B., & Wygant, J. R. (2019). Global survey and empirical model of fast magnetosonic waves over their full frequency range in Earth's inner magnetosphere. *Journal of Geophysical Research: Space Physics*, *124*(12), 10270–10282. <https://doi.org/10.1029/2019JA027407>
- Ma, Q., Li, W., Thorne, R. M., & Angelopoulos, V. (2013). Global distribution of equatorial magnetosonic waves observed by THEMIS. *Geophysical Research Letters*, *40*(10), 1895–1901. <https://doi.org/10.1002/grl.50434>
- Ma, Q., Li, W., Yue, C., Thorne, R. M., Bortnik, J., Kletzing, C. A., et al. (2019). Ion heating by electromagnetic ion cyclotron waves and magnetosonic waves in the Earth's inner magnetosphere. *Geophysical Research Letters*, *46*(12), 6258–6267. <https://doi.org/10.1029/2019GL083513>
- Maldonado, A. A., & Chen, L. (2018). On the diffusion rates of electron bounce resonant scattering by magnetosonic waves. *Geophysical Research Letters*, *45*(8), 3328–3337. <https://doi.org/10.1002/2017GL076560>
- Mauk, B. H., Fox, N. J., Kanekal, S. G., Kessel, R. L., Sibeck, D. G., & Ukhorskiy, A. (2013). Science objectives and rationale for the radiation belt storm probes mission. *Space Science Reviews*, *179*(1–4), 3–27. <https://doi.org/10.1007/s11214-012-9908-y>
- Meredith, N. P., Horne, R. B., & Anderson, R. R. (2008). Survey of magnetosonic waves and proton ring distributions in the Earth's inner magnetosphere. *Journal of Geophysical Research*, *113*(A6), A06213. <https://doi.org/10.1029/2007JA012975>
- Min, K., Denton, R. E., Liu, K., Gary, S. P., & Spence, H. E. (2017). Ion Bernstein instability as a possible source for oxygen ion cyclotron harmonic waves. *Journal of Geophysical Research: Space Physics*, *122*(5), 5449–5465. <https://doi.org/10.1002/2017JA023979>
- Olsen, R. C. (1981). Equatorially trapped plasma populations. *Journal of Geophysical Research*, *86*(A13), 11235–11245. <https://doi.org/10.1029/JA086A13p11235>
- Polo, J., Mackay, T., & Lakhtakia, A. (2013). *Electromagnetic surface waves: A modern perspective*. Newnes.
- Russell, C. T., Holzer, R. E., & Smith, E. J. (1970).OGO 3 observations of ELF noise in the magnetosphere. 2. The nature of the equatorial noise. *Journal of Geophysical Research*, *75*(4), 755–768. <https://doi.org/10.1029/JA075i004p00755>
- Santolík, O., Nemeč, F., Gereová, K., Macúšová, E., Conchy, Y., & Cornilleau-Wehrin, N. (2004). Systematic analysis of equatorial noise below the lower hybrid frequency. *Annales Geophysicae*, *22*(7), 2587–2595. <https://doi.org/10.5194/angeo-22-2587-2004>
- Santolík, O., Parrot, M., & Lefeuvre, F. (2003). Singular value decomposition methods for wave propagation analysis. *Radio Science*, *38*(1), 1010. <https://doi.org/10.1029/2000RS002523>
- Santolík, O., Parrot, M., & Němec, F. (2016). Propagation of equatorial noise to low altitudes: Decoupling from the magnetosonic mode. *Geophysical Research Letters*, *43*(13), 6694–6704. <https://doi.org/10.1002/2016GL069582>
- Santolík, O., Pickett, J. S., Gurnett, D. A., Maksimovic, M., & Cornilleau-Wehrin, N. (2002). Spatiotemporal variability and propagation of equatorial noise observed by Cluster. *Journal of Geophysical Research*, *107*(A12), 1495. <https://doi.org/10.1029/2001JA009159>
- Santolík, O., Pickett, J. S., Gurnett, D. A., Menietti, J. D., Tsurutani, B. T., & Verkhoglyadova, O. (2010). Survey of Poynting flux of whistler mode chorus in the outer zone. *Journal of Geophysical Research*, *115*(A7), A00F13. <https://doi.org/10.1029/2009JA014925>
- Santolík, O., Pickett, J. S., Gurnett, D. A., & Storey, L. R. O. (2002). Magnetic component of narrowband ion cyclotron waves in the auroral zone. *Journal of Geophysical Research*, *107*(A12), 1444. <https://doi.org/10.1029/2001JA000146>
- Shprits, Y. Y. (2016). Estimation of bounce resonant scattering by fast magnetosonic waves. *Geophysical Research Letters*, *43*(3), 998–1006. <https://doi.org/10.1002/2015GL066796>
- Sonwalkar, V. S. (2006). The influence of plasma density irregularities on whistler-mode wave propagation. In J. W. Labelle & R. A. Treumann (Eds.), *Geospace electromagnetic waves and radiation* (Vol. 687, p. 141).
- Spence, H. E., Reeves, G. D., Baker, D. N., Blake, J. B., Bolton, M., Bourdarie, S., et al. (2013). Science goals and overview of the radiation belt storm probes (RBSP) energetic particle, composition, and thermal plasma (ECT) suite on NASA's Van Allen Probes Mission. *Space Science Reviews*, *179*(1–4), 311–336. <https://doi.org/10.1007/s11214-013-0007-5>
- Streltsov, A. V., Lampe, M., Manheimer, W., Ganguli, G., & Joyce, G. (2006). Whistler propagation in inhomogeneous plasma. *Journal of Geophysical Research*, *111*(A3), A03216. <https://doi.org/10.1029/2005JA011357>
- Su, Z., Liu, N., Zheng, H., Wang, Y., & Wang, S. (2018). Large-amplitude extremely low frequency hiss waves in plasmaspheric plumes. *Geophysical Research Letters*, *45*(2), 565–577. <https://doi.org/10.1002/2017GL076754>
- Su, Z., Wang, G., Liu, N., Zheng, H., Wang, Y., & Wang, S. (2017). Direct observation of generation and propagation of magnetosonic waves following substorm injection. *Geophysical Research Letters*, *44*(15), 7587–7597. <https://doi.org/10.1002/2017GL074362>
- Sun, J., Gao, X., Lu, Q., Chen, L., Liu, X., Wang, X., et al. (2017). Spectral properties and associated plasma energization by magnetosonic waves in the Earth's magnetosphere: Particle-in-cell simulations. *Journal of Geophysical Research: Space Physics*, *122*(5), 5377–5390. <https://doi.org/10.1002/2017JA024027>
- Tao, X., & Li, X. (2016). Theoretical bounce resonance diffusion coefficient for waves generated near the equatorial plane. *Geophysical Research Letters*, *43*(14), 7389–7397. <https://doi.org/10.1002/2016GL070139>

- Thomas, N., Shiokawa, K., Miyoshi, Y., Kasahara, Y., Shinohara, I., Kumamoto, A., et al. (2021). Investigation of small scale electron density irregularities observed by the Arase and Van Allen Probes satellites inside and outside the plasmasphere. *Journal of Geophysical Research: Space Physics*, *126*(3), e27917. <https://doi.org/10.1029/2020JA027917>
- Tsurutani, B. T., Falkowski, B. J., Pickett, J. S., Verkhoglyadova, O. P., Santolik, O., & Lakhina, G. S. (2014). Extremely intense ELF magnetosonic waves: A survey of polar observations. *Journal of Geophysical Research*, *119*(2), 964–977. <https://doi.org/10.1002/2013JA019284>
- Williams, T. (2014). *Full-wave simulation of high-frequency electromagnetic propagation through inhomogeneous plasma (Unpublished doctoral dissertation)*. University of York.
- Woodroffe, J. R., & Streltsov, A. V. (2014). Whistler interaction with field-aligned density irregularities in the ionosphere: Refraction, diffraction, and interference. *Journal of Geophysical Research: Space Physics*, *119*(7), 5790–5799. <https://doi.org/10.1002/2013JA019683>
- Wu, Z., Su, Z., Goldstein, J., Liu, N., He, Z., Zheng, H., & Wang, Y. (2022). Nightside plasmaspheric plume-to-core migration of whistler-mode hiss waves. *Geophysical Research Letters*, *49*(16), e00306. <https://doi.org/10.1029/2022GL100306>
- Wu, Z., Su, Z., He, Z., Zheng, H., & Wang, Y. (2022). Magnetosonic Waves above the lower hybrid frequency in cyclotron resonance with the Van Allen radiation belt electrons. *Geophysical Research Letters*, *49*(23), e2022GL100971. <https://doi.org/10.1029/2022GL100971>
- Wu, Z., Su, Z., Liu, N., Gao, Z., Zheng, H., Wang, Y., & Wang, S. (2021). Off-equatorial source of magnetosonic waves extending above the lower hybrid resonance frequency in the inner magnetosphere. *Geophysical Research Letters*, *48*(6), e2020GL091830. <https://doi.org/10.1029/2020GL091830>
- Wygant, J. R., Bonnell, J. W., Goetz, K., Ergun, R. E., Mozer, F. S., Bale, S. D., et al. (2013). The electric field and waves instruments on the radiation belt storm probes mission. *Space Science Reviews*, *179*(1–4), 183–220. <https://doi.org/10.1007/s11214-013-0013-7>
- Xiao, F., Yang, C., Su, Z., Zhou, Q., He, Z., He, Y., et al. (2015). Wave-driven butterfly distribution of Van Allen belt relativistic electrons. *Nature Communications*, *6*(1), 8590. <https://doi.org/10.1038/ncomms9590>
- Xiao, F., Zhou, Q., He, Z., & Tang, L. (2012). Three-dimensional ray tracing of fast magnetosonic waves. *Journal of Geophysical Research*, *117*(A6), A06208. <https://doi.org/10.1029/2012JA017589>
- Xiao, F., Zhou, Q., He, Z., Yang, C., He, Y., & Tang, L. (2013). Magnetosonic wave instability by proton ring distributions: Simultaneous data and modeling. *Journal of Geophysical Research: Space Physics*, *118*(7), 4053–4058. <https://doi.org/10.1002/jgra.50401>
- Xu, X., Chen, L., Zhou, C., Liu, X., Xia, Z., Simpson, J. J., & Zhang, Y. (2020). Two-dimensional full-wave simulation of whistler mode wave propagation near the local lower hybrid resonance frequency in a dipole field. *Journal of Geophysical Research: Space Physics*, *125*(4), e27750. <https://doi.org/10.1029/2019JA027750>
- Yang, L., Xie, Y., & Yu, P. (2011). Study of bandgap characteristics of 2d magnetoplasma photonic crystal by using m-fdtd method. *Microwave and Optical Technology Letters*, *53*(8), 1778–1784. <https://doi.org/10.1002/mop.26143>
- Yu, J., Li, L. Y., Cui, J., Cao, J. B., & Wang, J. (2019). Effect of low-harmonic magnetosonic waves on the radiation belt electrons inside the plasmasphere. *Journal of Geophysical Research: Space Physics*, *124*(5), 3390–3401. <https://doi.org/10.1029/2018JA026328>
- Yu, X., Yuan, Z., Ouyang, Z., & Yao, F. (2021). Effects of the plasmopause on the radial propagation of fast magnetosonic waves: An analytical approach. *Journal of Geophysical Research: Space Physics*, *126*(3), e28330. <https://doi.org/10.1029/2020JA028330>
- Yu, X., Yuan, Z., Yao, F., Ouyang, Z., & Wang, D. (2021). Electromagnetic characteristics of fast magnetosonic waves in the inner magnetosphere. *Journal of Geophysical Research: Space Physics*, *126*(9), e29759. <https://doi.org/10.1029/2021JA029759>
- Yu, X., Yuan, Z., & Yu, J. (2020). Revisit the analytical approximation of transit-time scattering for fast magnetosonic waves. *Geophysical Research Letters*, *47*(16), e88434. <https://doi.org/10.1029/2020GL088434>
- Yuan, Z., Ouyang, Z., Yu, X., Huang, S., Yao, F., & Funsten, H. O. (2018). Global distribution of proton rings and associated magnetosonic wave instability in the inner magnetosphere. *Geophysical Research Letters*, *45*(19), 10160–10166. <https://doi.org/10.1029/2018GL079999>
- Yuan, Z., Yu, X., Huang, S., Qiao, Z., Yao, F., & Funsten, H. O. (2018). Cold ion heating by magnetosonic waves in a density cavity of the plasmasphere. *Journal of Geophysical Research: Space Physics*, *123*(2), 1242–1250. <https://doi.org/10.1002/2017JA024919>